ELSEVIER
Available online at www.sciencedirect.com
SCIENCE DIRECT®
Journal of Catalysis 235 (2005) 368–377
JOURNAL OF CATALYSIS
www.elsevier.com/locate/jcat

Effects of cerium incorporation into zirconia on the activity of Cu/ZrO_2 for methanol synthesis via CO hydrogenation

Konstantin A. Pokrovski, Michael D. Rhodes, Alexis T. Bell [*]

Chemical Sciences Division, Lawrence Berkeley National Laboratory and Department of Chemical Engineering, University of California, Berkeley, CA 94720-1462, USA

Received 18 May 2005; revised 25 August 2005; accepted 1 September 2005

Abstract

The effects of Ce incorporation into ZrO_2 on the catalytic performance of Cu/ZrO_2 for the hydrogenation of CO were investigated. A $Ce_{0.3}Zr_{0.7}O_2$ solid solution was synthesized by forced hydrolysis at low pH. After calcination at 873 K, X-ray diffraction and Raman spectroscopy characterization indicated that the $Ce_{0.3}Zr_{0.7}O_2$ had a t'' crystal structure. It was found that 1.2 wt% Cu/$Ce_{0.3}Zr_{0.7}O_2$ exhibited H_2 consumption peaks at low temperature (<473 K) during H_2-TPR, indicating that a significant fraction ($\sim 70\%$) of Ce^{4+} is reduced to Ce^{3+}. The 1.2 wt% Cu/$Ce_{0.3}Zr_{0.7}O_2$ is 2.7 times more active for methanol synthesis than 1.2 wt% Cu/m-ZrO_2 at 3.0 MPa at temperatures between 473 and 523 K and exhibits a higher selectivity to methanol. In situ infrared spectroscopy shows that, analogous to Cu/m-ZrO_2, the primary surface species on Cu/$Ce_{0.3}Zr_{0.7}O_2$ during CO hydrogenation are formate and methoxide species. A shift in the band position of the bridged methoxide species indicated that some of these groups were bonded to both Zr^{4+} and Ce^{3+} cations. For both catalysts, the rate-limiting step for methanol synthesis is the reductive elimination of methoxide species. The higher rate of methanol synthesis on Cu/$Ce_{0.3}Zr_{0.7}O_2$ relative to Cu/m-ZrO_2 was due primarily to a ~ 2.4 times higher apparent rate constant, k_{app}, for methoxide hydrogenation, which is attributed to the higher surface concentration of H atoms on the former catalyst. The increased capacity of the Ce-containing catalyst is attributed to interactions of H atoms with Ce–O pairs present at the surface of the oxide phase.

Keywords: Methanol synthesis; Cu; ZrO_2; CO hydrogenation; Ce

1. Introduction

Several studies have indicated that support composition affects the activity of Cu-based catalysts for CO hydrogenation to methanol [1–6]. Zirconia has proven a particularly promising support for such applications, because Cu/ZrO_2 catalysts can be operated with or without the presence of CO_2 [7–11]. Mechanistic studies have shown that for such catalysts, CO adsorbs preferentially on the surface of zirconia to form formate species, which then undergo hydrogenation to produce methanol. The hydrogen atoms required for this process are produced by dissociative adsorption of H_2 on the surface of the dispersed Cu and then spill over onto the zirconia surface. Recent work by Bell et al. [12,13] has demonstrated that the phase of zirconia can also influence catalyst activity. Thus Cu/m-ZrO_2 (m-ZrO_2, monoclinic zirconia) was shown to be nearly an order of magnitude more active for methanol synthesis than Cu/t-ZrO_2 (t-ZrO_2, tetragonal zirconia) for equivalent zirconia surface areas and surface concentrations of dispersed Cu. This difference is attributed primarily to the presence of oxygen vacancies on the surface of m-ZrO_2, which facilitate the reaction of CO with neighboring hydroxyl groups to generate formate species and provide additional sites for hydrogen activation and storage. These properties result in higher CO adsorption capacities and higher rates of reductive elimination of methoxide species on Cu/m-ZrO_2 relative to Cu/t-ZrO_2. Because the availability of atomic H on the surface of zirconia is essential for the hydrogenation of adsorbed CO, a motivation exists for exploring ways to increase the hydrogen adsorption capacity of zirconia.

CeO_2 has been used in automotive three-way catalysts to serve as an oxygen-buffering component during rich/lean oscillations of exhaust gases [14–18]. The ability of CeO_2 to either

---

[*] Corresponding author.
E-mail address: bell@cchem.berkeley.edu (A.T. Bell).

0021-9517/$ – see front matter © 2005 Elsevier Inc. All rights reserved.
doi:10.1016/j.jcat.2005.09.002

donate its oxygen or adsorb and store oxygen derived from molecular sources stems from the facile, reversible redox cycle $Ce^{4+} \rightleftarrows Ce^{3+}$. Reduction of CeO_2 to CeO_{2-x} stoichiometries results in the generation of oxygen vacancies throughout the oxide lattice. Incorporation of Zr^{4+} into the CeO_2 lattice enhances reducibility and increases the oxygen-storage capacity of the solid solution [14,15,17,19]. Spectroscopic studies suggest that the coordination number of the smaller Zr ion decreases in the mixed oxide, increasing oxygen mobility and the creation of vacancies [20].

The present study was undertaken to examine the influence of Ce incorporation into ZrO_2 on the catalytic activity of $Cu/Ce_xZr_{1-x}O_2$ for methanol synthesis from CO/H_2. ZrO_2 and $Ce_{0.3}Zr_{0.7}O_2$ were prepared by forced hydrolysis at low pH and Cu was dispersed on the surface of these materials by deposition precipitation. Catalysts were characterized by X-ray diffraction (XRD), Raman spectroscopy, and temperature-programmed reduction (TPR) in H_2, and catalyst H_2 and CO adsorption capacities were measured by temperature-programmed desorption (TPD). Steady-state catalytic performance measurements were supplemented with dynamic surface studies using in situ infrared spectroscopy.

2. Experimental

2.1. Catalyst preparation

ZrO_2 was prepared by boiling a 0.5-M solution of zirconyl chloride ($ZrOCl_2 \cdot 8H_2O$, 99.99%, Aldrich) under reflux for 240 h. The final solution had a $pH < 1$. NH_4OH was added dropwise to agglomerate the resulting fine particles, to facilitate their filtration. The recovered precipitate was washed and redispersed in deionized water several times to remove residual chlorine. $AgNO_3$ was used to test the filtrate for any remaining Cl anions. The material was then dried in air at 383 K overnight before calcination. $Ce_{0.3}Zr_{0.7}O_2$ was prepared by boiling a 0.5-M solution (total metals basis) of zirconyl nitrate [$ZrO(NO_3)_2 \cdot 6H_2O$, 99.99%, Aldrich] and cerium(III) nitrate [$Ce(NO_3)_3 \cdot 6H_2O$, 99.999%, Aldrich] under reflux for 240 h. The final solution had a $pH < 1$. NH_4OH was added dropwise to agglomerate the resulting fine particles to facilitate their filtration. The precipitated material was washed and then dried overnight before calcination. Each sample was calcined in dry air flowing at 100 cm^3/min. The temperature was ramped from room temperature at a rate of 2 K/min to the final temperature, which was maintained for 3 h. The ZrO_2 and $Ce_{0.3}Zr_{0.7}O_2$ samples were calcined at 738 and 873 K, respectively. Then 1.2 wt% Cu/ZrO_2 catalysts were prepared with each calcined support by deposition precipitation as described previously [12].

Before testing or characterization, each catalyst sample was calcined in a 10% O_2/He mixture flowing at 60 cm^3/min. The sample was heated from room temperature to 573 K at 0.5 K/min and maintained at 573 K for 2 h. The sample was then cooled to 323 K, swept with He, and reduced in a 10% H_2/He mixture at a flow rate of 60 cm^3/min while increasing the temperature by 2 K/min up to 573 K. The 10% H_2/He flow was maintained at 573 K for 1 h before switching to a flow of 100% H_2 for an additional 1 h.

2.2. Catalyst characterization

The crystallographic phase of each material was determined by both XRD and Raman spectroscopy. XRD patterns were obtained with a Siemens D5000 diffractometer, using Cu-K_α radiation and a graphite monochrometer. Scans were made in the 2θ range of 10° to 120° with a step size of 0.02° and a time/step of 11 s. Rietveld refinement was performed using EXPGUI GSAS software [21]. Raman spectra were recorded with a HoloLab 5000 Raman spectrometer (Kaiser Optical) at room temperature at a resolution of 2 cm^{-1}. The stimulating light source was a Nd:YAG laser, the output of which was frequency doubled to 532 nm. Laser power at the sample was approximately 20 mW.

The BET surface area of each ZrO_2 support was determined using an Autosorb 1 (Quantachrome Instruments) gas adsorption system with nitrogen adsorption/desorption isotherms. Before each analysis, samples were dried at 393 K under vacuum for >2 h. BET surface areas were calculated using a five-point isotherm. After calcination, the surface areas of ZrO_2 and $Ce_{0.3}Zr_{0.7}O_2$ were 143 and 120 m^2/g, respectively.

The concentration of exchangeable hydrogen on each sample was quantified using H/D exchange. Fully reduced samples were purged with He at 298 K for 30 min, followed by temperature ramping at 20 K/min from 298 to 623 K in 40 cm^3/min of D_2. Both HD and H_2 evolution were monitored using a mass spectrometer (Minilab, Spectra Products), but only HD generation was observed. For each sample, exchange was complete by $\sim$523 K.

H_2-TPR studies were conducted using 0.15 g of a calcined sample purged with He at 298 K for 30 min. The flow was switched to 2% H_2/He at a flow rate of 60 cm^3/min and then ramped from 298 to 673 K while monitoring H_2 consumption using a mass spectrometer. Cu surface areas were quantified using N_2O titrations followed by H_2-TPR [22]. A value of 1.46×10^{19} Cu atoms/m^2 and a stoichiometry of 2 Cu/H_2 was used [23].

Adsorption capacities for H_2 and CO and were determined using TPD. In the case of H_2 the sample was calcined and reduced at 573 K. The sample was then cooled in H_2 to 298 K and purged in He. Desorption was conducted by ramping the sample temperature at 20 K/min from 298 to 773 K in flowing He while monitoring the desorbing gas using a mass spectrometer. To determine the CO adsorption capacity, the sample was calcined and reduced, then cooled to 523 K and flushed with He for 30 min. Then 4.0% CO/He was flowed over the catalyst at a flow rate of 60 cm^3/min for 20 min. The sample was then cooled to 298 K in 4.0% CO/He before being purged with He to remove any weakly adsorbed species. Desorption of adsorbed CO was carried out in a manner identical to that used for adsorbed H_2.

2.3. Catalyst testing

Activity and selectivity measurements for CO hydrogenation were carried out in a continuous-flow, fixed-bed reactor as described previously [12]. Reactions were carried out with 0.15 g of catalyst at a pressure of 3.0 MPa. Total reactant gas flow was 60 cm^3/min, with a H_2/CO ratio of 3/1. Product gas mixtures were analyzed after 2 h on stream at a given temperature. Temperature was then ramped to the successive temperature at a rate of 2 K/min. Conversion and selectivity were referenced to CO, the limiting reactant.

2.4. Infrared spectroscopy studies

In situ transmission infrared spectroscopy experiments were conducted using a low-dead volume infrared cell with CaF_2 windows [24]. Infrared spectra were recorded with Magna 750 Series II IR spectrometer (Nicolet) at a resolution of 2 cm^{-1}. In an effort to remove any residual surface species before testing, each sample was calcined in a 10% O_2/He mixture flowing at 60 cm^3/min. The sample was heated from room temperature to 523 K at 2 K/min and maintained at 523 K for 8 h. The sample was then cooled to 323 K, swept with He, and reduced in a 10% H_2/He mixture at a flow rate of 60 cm^3/min while increasing the temperature at the rate of 2 K/min up to 523 K. The flow of 10% H_2/He was maintained at 523 K for 1 h before switching to a flow of 100% H_2 for an additional 1–3 h. The sample was then flushed with He for 1 h before sample testing.

3. Results and discussion

3.1. Material characterization of ZrO_2 supports

XRD patterns of the ZrO_2 and $Ce_{0.3}Zr_{0.7}O_2$ are shown in Fig. 1. The diffraction pattern for ZrO_2 exhibited peaks characteristic of monoclinic ZrO_2 (m-ZrO_2). The occurrence of pure monoclinic ZrO_2 was confirmed by Rietveld refinement in the monoclinic symmetry, $P2_1/c$ (Figs. 1d and e). The XRD pattern for $Ce_{0.3}Zr_{0.7}O_2$ exhibited a primary diffraction peak centered at $2\theta \sim 30°$, characteristic of both the tetragonal and cubic phases of ZrO_2 (t-ZrO_2 and c-ZrO_2, respectively) (Fig. 1a). The position of the main peak, $Ce_{0.3}Zr_{0.7}O_2$, occurred at 29.5°, as opposed to 30.2° for t-ZrO_2 and c-ZrO_2, consistent with an increase in the lattice cell parameter with the substitution of Zr^{4+} (radius 0.86 Å) by Ce^{4+} cations (radius 0.97 Å). The symmetry of the diffraction peaks and the absence of features associated with CeO_2 suggest the formation of a $Ce_xZr_{1-x}O_2$ solid solution [25,26]. The thermodynamically stable phase of $Ce_xZr_{1-x}O_2$ solutions is monoclinic for Zr-rich compositions (<10 at% Ce) and cubic for Ce-rich compositions (>80 at% Ce) [27,28]. Intermediate compositions are reported to exhibit a number of stable and metastable phases of tetragonal symmetry [29–31]. The phase of $Ce_{0.3}Zr_{0.7}O_2$ was analyzed by Rietveld refinement of the measured diffraction pattern. Refinement was performed in both cubic ($Fm3m$, $a = 5.20$ Å) and tetragonal ($P4_2/nmc$, $a = 3.68$, $c = 5.19$, $a_f/c = 1.00(3)$, where $a_f = a\sqrt{2}$) symmetries (Figs. 1b and c, respectively). The broadness of the diffraction peaks made it impossible to identify the displacement of oxygen ions from their ideal fluorite positions by Rietveld refinement; hence a more definitive assessment of the crystalline structure of $Ce_{0.3}Zr_{0.7}O_2$ was attempted using Raman spectroscopy [32].

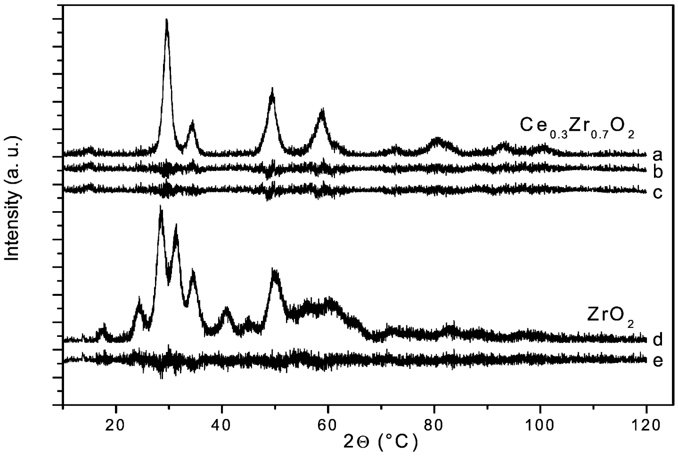

Fig. 1. XRD patterns for ZrO_2 and $Ce_{0.3}Zr_{0.7}O_2$. (a) Observed profile for $Ce_{0.3}Zr_{0.7}O_2$, (b) and (c) difference between observed and calculated profiles in cubic symmetry, $Fm3m$ space group, and tetragonal symmetry, $P4_2/nmc$ space group, respectively; (d) observed profile for ZrO_2; and (e) difference between observed and calculated profiles in monoclinic symmetry $P2_1/c$ space group).

The Raman spectra of ZrO_2 and $Ce_{0.3}Zr_{0.7}O_2$ are presented in Fig. 2. ZrO_2 exhibited peaks at 182, 333, 377, 475, 559, and 623 cm^{-1}, characteristic of m-ZrO_2 [33–35]. Thus both XRD and Raman spectroscopy confirmed that the ZrO_2 sample was m-ZrO_2. The $Ce_{0.3}Zr_{0.7}O_2$ sample exhibited a principle peak at 474 cm^{-1} and two smaller peaks at 316 and 621 cm^{-1}. The peak at 474 cm^{-1} was characteristic of a cubic fluorite structure [36,37]; however, the presence of peaks at 316 and 621 cm^{-1} and the absence of the characteristic tetragonal peak at ~275 cm^{-1} indicated that $Ce_{0.3}Zr_{0.7}O_2$ was in the t'' phase [29]. This phase is intermediate between the tetrago-

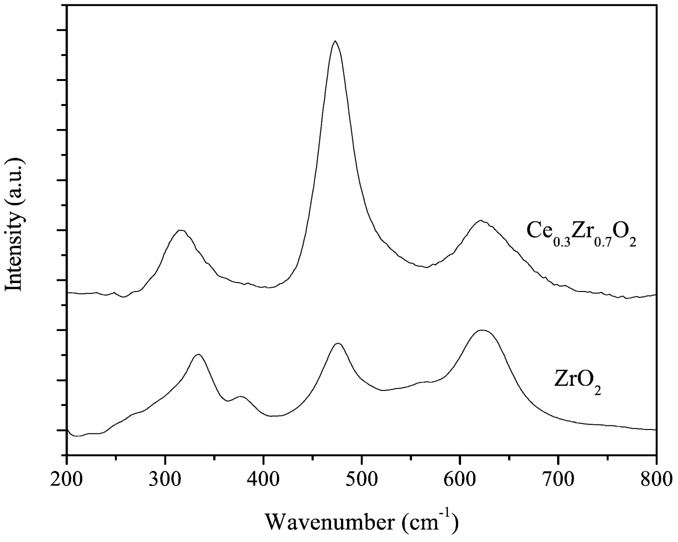

Fig. 2. Raman spectra for ZrO_2 and $Ce_{0.3}Zr_{0.7}O_2$ at room temperature.

Table 1
Cu surface area and exchangeable H for 1.2 wt% Cu/m-ZrO_2 and 1.2 wt% Cu/$Ce_{0.3}Zr_{0.7}O_2$

Sample	Cu surface area (m^2/g)	Cu dispersion (%)	Exchangeable H (µmol/m^2)
1.2 wt% Cu/m-ZrO_2	0.87	11.1	10.9
1.2 wt% Cu/$Ce_{0.3}Zr_{0.7}O_2$	0.73	9.3	7.8

nal and cubic phases, in which the oxygen atoms are displaced from the positions of these atoms in an ideal fluorite structure. Whereas the t'' phase is commonly reported to exist at Ce compositions between 65 and 80 at% [29], others have reported the generation of this phase at lower Ce content for small particles [38,39].

3.2. Material characterization of Cu/m-ZrO_2 and Cu/t''-$Ce_{0.3}Zr_{0.7}O_2$

A loading of 1.2 wt% Cu was deposited onto ZrO_2 and $Ce_{0.3}Zr_{0.7}O_2$. The Cu surface area and associated dispersion for each sample are given in Table 1. The Cu particles dispersed on m-ZrO_2 had a slightly higher overall Cu surface area, but each catalyst had a very similar Cu surface area to support surface area ratio. The surface concentration of exchangeable hydrogen for each sample, quantified by H/D exchange, is also listed in Table 1. In situ infrared studies have shown that this quantity indicates the concentration of hydroxyl groups on the catalyst surface [40,41]. The surface concentration of OH groups was ~40% higher on 1.2 wt% Cu/m-ZrO_2 than on 1.2 wt% Cu/$Ce_{0.3}Zr_{0.7}O_2$. The infrared spectra of the O–H stretching region after calcination and reduction for 1.2 wt% Cu/m-ZrO_2 and 1.2 wt% Cu/$Ce_{0.3}Zr_{0.7}O_2$ are shown in Fig. 3. The spectra were referenced to the empty cell in He. Each sample exhibited two types of isolated hydroxyl groups (>3600 cm^{-1}). Despite a pseudo-tetragonal/cubic crystal structure, the peak positions of 1.2 wt% Cu/$Ce_{0.3}Zr_{0.7}O_2$ (3670 and 3731 cm^{-1}) were very similar to those for 1.2 wt% Cu/m-ZrO_2 (3668 and 3729 cm^{-1}). Analogous to 1.2 wt% Cu/m-ZrO_2, 1.2 wt% Cu/t''-$Ce_{0.3}Zr_{0.7}O_2$ exhibited a higher relative concentration of low-frequency hydroxyl groups. The positions of these features were similar to those reported previously for OH bands on t-ZrO_2 and m-ZrO_2 [39–41]. Although the exact positions of such bands can depend on the degree of surface hydroxylation, the higher-frequency band is commonly assigned to terminal hydroxyl groups, and the lower-frequency band is commonly assigned to either bi- or tri-bridging groups [40,42]. Recent theoretical studies of the surfaces of both ZrO_2 polymorphs also lead to the conclusion that a combination of terminal and both bi- and tri-bridged OH groups should be present [43–46].

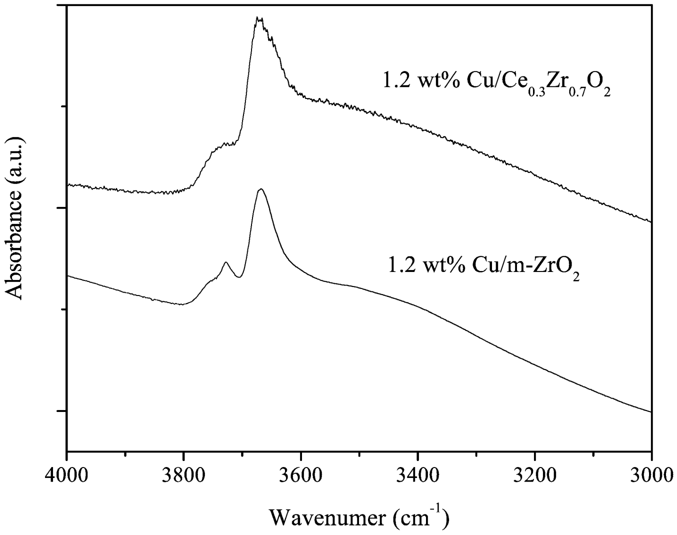

Fig. 3. Infrared spectra of the hydroxyl group stretching region taken for 1.2 wt% Cu/ZrO_2 and 1.2 wt% Cu/$Ce_{0.3}Zr_{0.7}O_2$ following calcination and reduction. Spectra referenced to empty cell in He.

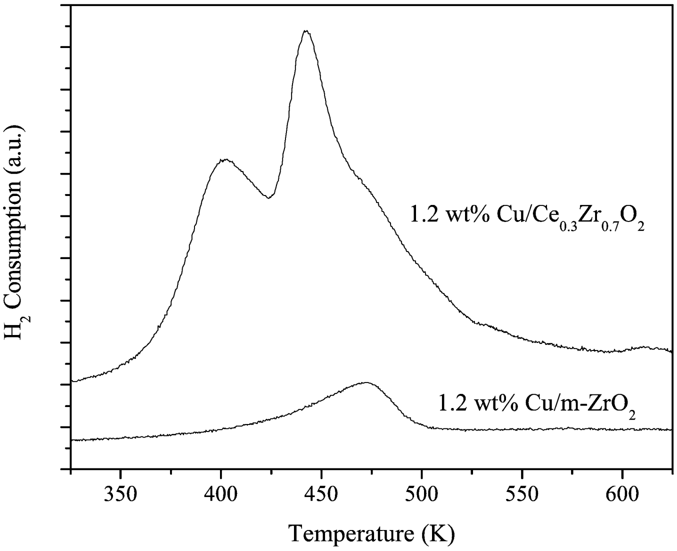

Fig. 4. H_2-TPR spectra for 1.2 wt% Cu/m-ZrO_2 and 1.2 wt% Cu/$Ce_{0.3}Zr_{0.7}O_2$. Heating rate = 20 K/min; 2% H_2/He flow rate = 60 cm^3/min.

The H_2-TPR profiles for the catalysts are shown in Fig. 4. The 1.2 wt% Cu/m-ZrO_2 exhibited one principle peak with a maximum at 473 K, attributed to the reduction of highly dispersed CuO or Cu^{2-} ions in an octahedral environment [42,43]. The amount of H_2 consumed was slightly greater than the value corresponding to the complete reduction of CuO species ($H_2/CuO \approx 1.1$). The 1.2 wt% Cu/t''-$Ce_{0.3}Zr_{0.7}O_2$ exhibited significantly greater H_2 consumption, due to the reduction of Ce^{4+} to Ce^{3+}. If the H_2/CuO ratio is assumed to be ~1, then the additional H_2 consumption corresponds to a reduction of ~70% of the Ce atoms in the support. Reduction occurs with two primary peaks at 403 and 443 K. The presence of either noble or base metals facilitates reduction of Ce because of spillover of H atoms from the metal surface [44–46]. Similar reduction peaks have been reported during H_2-TPR with $CuO/Ce_{0.44}Zr_{0.56}O_2$ [47].

Table 2 lists the H_2 and CO adsorption capacities of 1.2 wt% Cu/m-ZrO_2 and 1.2 wt% Cu/t''-$Ce_{0.3}Zr_{0.7}O_2$ determined from TPD spectra. The amount of H_2 adsorbed per unit area was 3.3 times higher for 1.2 wt% Cu/t''-$Ce_{0.3}Zr_{0.7}O_2$ than for 1.2 wt% Cu/m-ZrO_2. Although the total amount of CO adsorbed was significantly higher than the amount of H_2 adsorbed on both catalysts, the ratio of CO adsorbed on 1.2 wt% Cu/t''-

Table 2
Effect of Ce incorporation on the adsorption capacity and binding strength of CO at 523 K

Sample	CO desorbed (μmol/m^2)	Peak max. T (K)	CO_2 desorbed (μmol/m^2)	Peak max. T (K)	Total CO_x desorbed (μmol/m^2)	H_2 desorbed (μmol/m^2)
1.2 wt% Cu/m-ZrO_2	0.51	620	0.77	590, 675	1.28	0.26
1.2 wt% Cu/$Ce_{0.3}Zr_{0.7}O_2$	0.94	575, 615	0.60	635	1.54	0.87

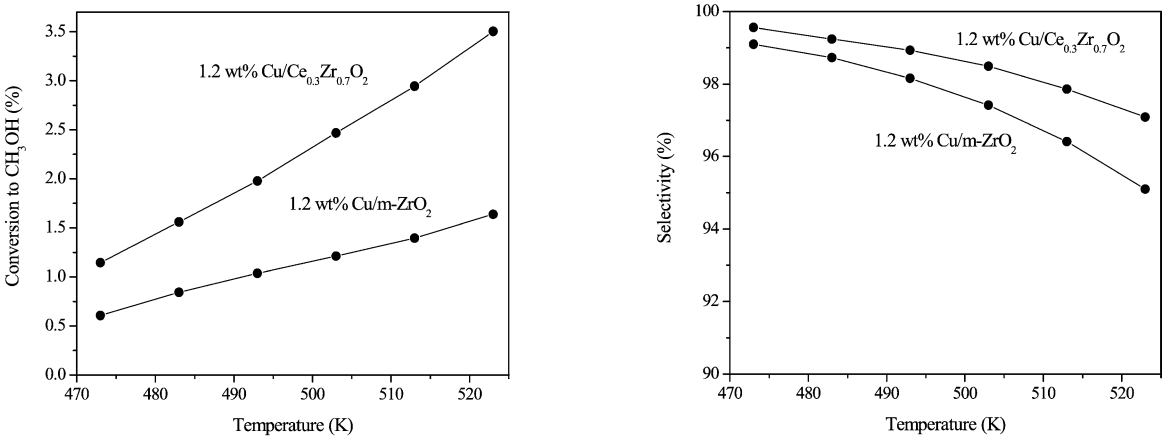

(a) (b)

Fig. 5. Effect of temperature on the selective conversion (a) and overall selectivity (b) of CO to methanol during CO hydrogenation: catalyst mass, 0.15 g; $p = 3.0$ MPa; $H_2/CO = 3$; total flow rate, 60 cm^3/min.

$Ce_{0.3}Zr_{0.7}O_2$ relative to that on 1.2 wt% Cu/m-ZrO_2 was only a factor of 1.2. Thus it is apparent that the dominant effect of incorporating Ce into the zirconia lattice is to increase the H_2 adsorption capacity of the oxide. Although the physical reason for this effect is not known, we propose that it may be due to the increased ability of Ce–O bonds in the oxide to stabilize H atoms as $H^{\delta-}$ and $H^{\delta+}$ species [48,49].

3.3. *Catalytic performance of Cu/m-ZrO_2 and Cu/t″-$Ce_{0.3}Zr_{0.7}O_2$*

The effects of reaction temperature on the activity and selectivity of the 1.2 wt% Cu/m-ZrO_2 and 1.2 wt% Cu/t''-$Ce_{0.3}Zr_{0.7}O_2$ catalysts are shown in Fig. 5. Conversion to methanol increased over the temperature range 473–523 K and was accompanied by a decrease in selectivity. The only major byproduct observed was methane. These conversion levels were far below the equilibrium values for the given temperatures, indicating that the observed rate of methanol formation was not influenced by methanol decomposition. The 1.2 wt% Cu/t''-$Ce_{0.3}Zr_{0.7}O_2$ catalyst exhibited higher conversion to methanol than the m-ZrO_2 supported catalysts over the temperature range studied; for example, the methanol productivity of 1.2 wt% Cu/t''-$Ce_{0.3}Zr_{0.7}O_2$ was approximately double that of 1.2 wt% Cu/m-ZrO_2 at 523 K. The higher activity of the $Ce_{0.3}Zr_{0.7}O_2$-supported catalyst was also accompanied by a greater selectivity to methanol.

3.4. *Infrared spectroscopy studies*

The nature of surface species and the dynamics of CO adsorption and hydrogenation were studied using in situ infrared spectroscopy. Fig. 6 shows spectra obtained during CO adsorption on 1.2 wt% Cu/m-ZrO_2 at 523 K. The catalyst was exposed to a flow of 15% CO/He at a total pressure of 0.50 MPa. The bands observed at 1563, 1386, and 1366 cm^{-1} can be attributed to the ν_{as}(OCO), δ(CH), and ν_s(OCO) modes of b-HCOO–Zr, respectively [2,5,50–56]. Accompanying features for b-HCOO–Zr in the CH stretching region occurred at 2969, 2883 cm^{-1}, and 2748 cm^{-1}, characteristic of [ν_{as}(OCO) + δ(CH)] [49,50,53], ν(CH) [2,5,46–51], and [ν_s(OCO) + δ(CH)] [54,57], respectively. C–H stretching features attributed to CH_3O–Zr (2934 and 2830 cm^{-1}) [4,37, 50,51,53,55,58,59] appeared almost immediately, even in the absence of gas phase H_2. These features continued to increase for the duration of the CO adsorption experiment (~1 h). At the same time, bands at 1039 and 1142 cm^{-1} appeared and increased in intensity at a rate similar to that for the bands at 2934 and 2830 cm^{-1}. These peaks were assigned to C–O stretching vibrations of terminal (t-OCH_3) and bridged (b-OCH_3) methoxide species on ZrO_2, respectively [58,60,61]. The shoulder located at approximately 1320 cm^{-1} was assigned to b-CO_3^{2-}–Zr species [41,56].

Fig. 7 shows spectra obtained during CO adsorption on 1.2 wt% Cu/$Ce_{0.3}Zr_{0.7}O_2$ at 523 K. The catalyst was exposed to a flow of 15% CO/He at a total pressure of 0.50 MPa. As for the 1.2 wt% Cu/m-ZrO_2, here the primary bands can be attributed to bidentate formate species with features at 1576, 1379, 1370, 2966, and 2878 cm^{-1}. Each band shifted relative to the position on pure ZrO_2, but bands reported for formate species on CeO_2 were noticeably absent [62–66]. A comparison with Fig. 6 reveals that formate species were formed at a faster rate on 1.2 wt% Cu/$Ce_{0.3}Zr_{0.7}O_2$. Methoxide species features at 1143, 1040, 2934, and 2828 cm^{-1} were nearly coinci-

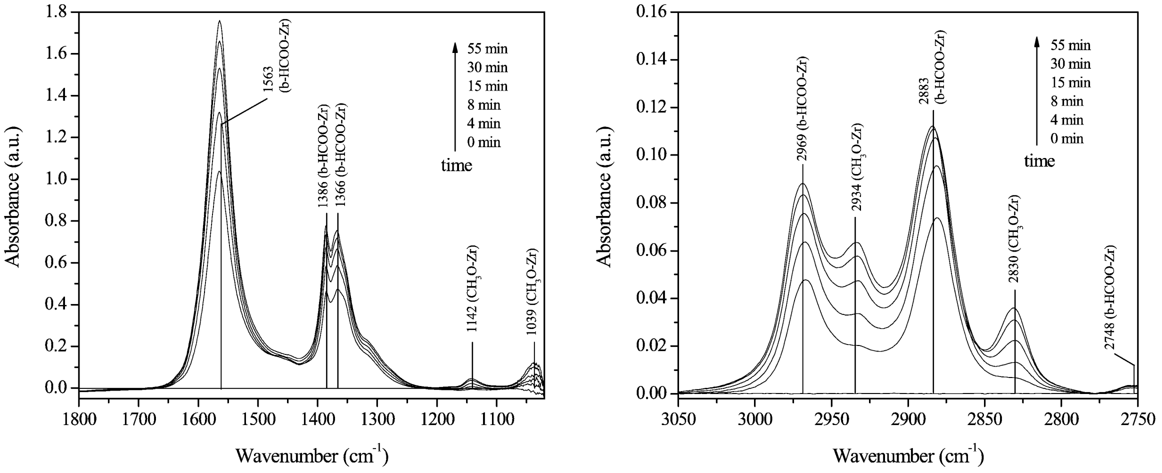

Fig. 6. Infrared spectra taken for 1.2 wt% Cu/m-ZrO_2 at 523 K after switching feed from 0.50 MPa He to 0.05 MPa CO and 0.45 MPa He flowing at a total rate of 60 cm^3/min. Spectra referenced to 1.2 wt% Cu/m-ZrO_2 under 0.50 MPa He flow at 523 K.

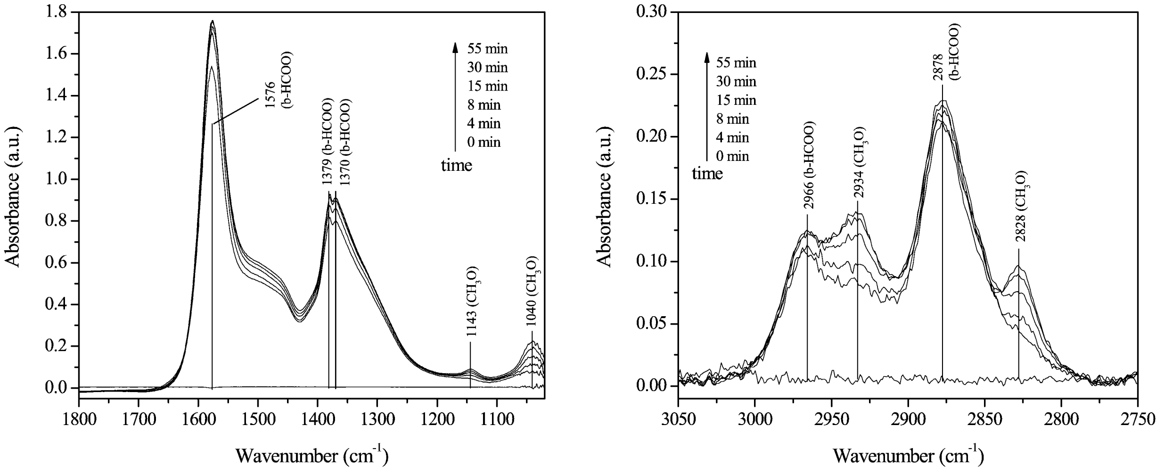

Fig. 7. Infrared spectra taken for 1.2 wt% Cu/$Ce_{0.3}Zr_{0.7}O_2$ at 523 K after switching feed from 0.50 MPa He to 0.05 MPa CO and 0.45 MPa He flowing at a total rate of 60 cm^3/min. Spectra referenced to 1.2 wt% Cu/$Ce_{0.3}Zr_{0.7}O_2$ under 0.50 MPa He flow at 523 K.

dent with those observed on 1.2 wt% Cu/m-ZrO_2 and increased over the duration of the transient. In addition to formate and methoxide species, the appearance of broad features at ∼1550–1450 and 1350–1250 cm^{-1} is indicative of various carbonate and carboxylate species [54,67], suggesting that the presence of Ce favors the formation of these species. Similar broad bands have been observed after CO adsorption at high temperature on CeO_2 [67].

After CO adsorption for 1 h, transient response spectra were obtained during CO hydrogenation by introducing H_2 into the flowing 15% CO/He (total pressure = 0.50 MPa) to achieve a H_2/CO ratio of 3/1. Fig. 8 shows spectra obtained on 1.2 wt% Cu/m-ZrO_2 after the switch at 523 K. The features of b-HCOO–Zr at 1564, 1385, and 1367 cm^{-1} decreased rapidly in intensity as soon as H_2 was introduced and simultaneously peaked for CH_3O–Zr at 1147 and 1047 cm^{-1}. In the C–H stretching region, bands for CH_3O–Zr increased until reaching a steady-state level after approximately 80 min, analogous to the pattern observed for the corresponding C–O stretching vibrations. During CO hydrogenation, each C–H stretch red shifted approximately 1015 cm^{-1} whereas each C–O stretch blue shifted approximately 3–8 cm^{-1}, presumably due to interactions between surface species with increasing surface coverage. The δ(CH) feature for CH_3O–Zr (1446 cm^{-1}) [5,54,58] was evident initially but remained relatively small throughout the transient.

Fig. 9 shows transient response spectra obtained during CO hydrogenation on 1.2 wt% Cu/t''-$Ce_{0.3}Zr_{0.7}O_2$ at 523 K. Spectra were obtained by introducing H_2 into the flowing 15% CO/He (total pressure = 0.50 MPa) to achieve a H_2/CO ratio of 3/1. After the introduction of H_2, the broad bands ascribable to carbonate and carboxylate species decreased rapidly. The features for b-HCOO at 1576, 1379, and 1370 cm^{-1} generally decreased over the course of the transient, whereas CH_3O features at 1148, 1061, 2923, and 2816 cm^{-1} increased rapidly and then approached steady-state levels. The ν(CO) mode of terminal CH_3O species was nearly coincident with that observed with m-ZrO_2, but the ν(CO) mode of bridged CH_3O species occurred at a higher wave number (1061 vs. 1047 cm^{-1}). Binet et al. [68,69] reported C–O stretches of bridged CH_3O species on Ce^{3+} sites at ∼1080 cm^{-1}. Because H_2-TPR demonstrates that most surface Ce^{4+} cations are reduced to Ce^{3+}, the upward shift of the bridged ν(CO) mode likely reflects the presence

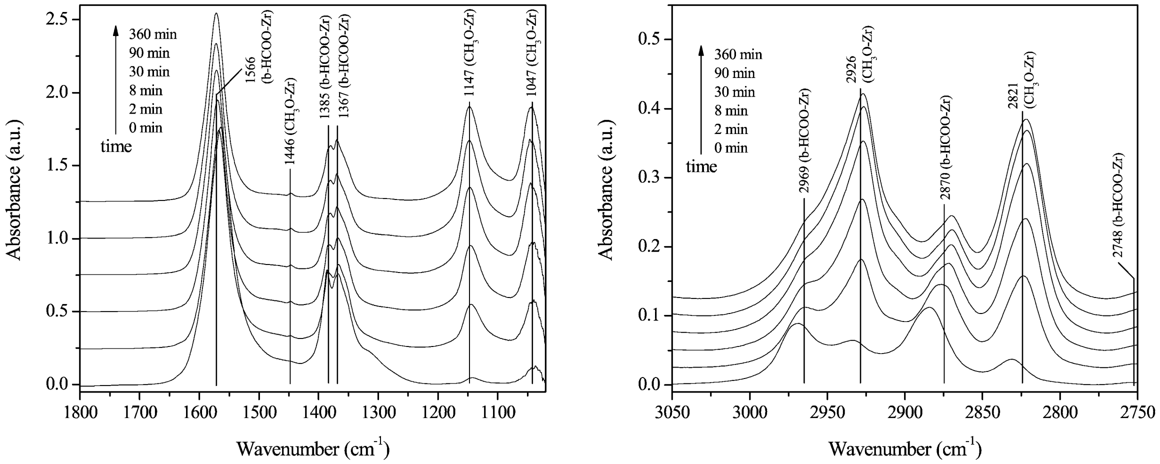

Fig. 8. Infrared spectra taken for 1.2 wt% Cu/*m*-ZrO_2 at 523 K after switching feed from 0.05 MPa CO and 0.45 MPa He to 0.05 MPa CO, 0.15 MPa H_2, and 0.30 MPa He flowing at a total rate of 60 cm^3/min. Spectra referenced to 1.2 wt% Cu/*m*-ZrO_2 under 0.50 MPa He flow at 523 K.

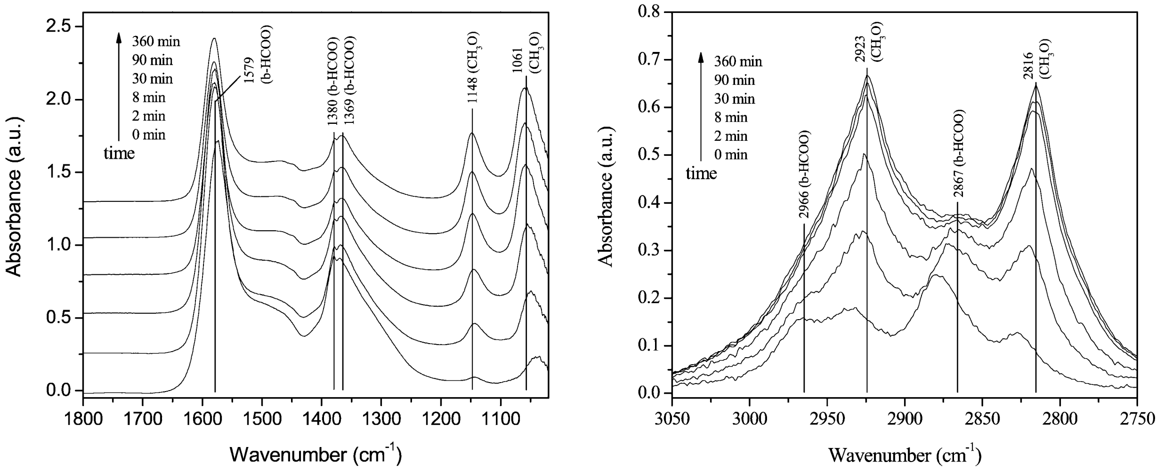

Fig. 9. Infrared spectra taken for 1.2 wt% Cu/$Ce_{0.3}Zr_{0.7}O_2$ at 523 K after switching feed from 0.05 MPa CO and 0.45 MPa He to 0.05 MPa CO, 0.15 MPa H_2, and 0.30 MPa He flowing at a total rate of 60 cm^3/min. Spectra referenced to 1.2 wt% Cu/$Ce_{0.3}Zr_{0.7}O_2$ under 0.50 MPa He flow at 523 K.

of methoxide species bonded to both Zr^{4+} and Ce^{3+} cations. Consistent with a reduction of most of the Ce atoms in the $Ce_{0.3}Zr_{0.7}O_2$ lattice, no terminal CH_3O was observed on Ce^{4+} cations at ~1105 cm^{-1} [68,69].

Fig. 10 compares the evolution of the principle surface species on 1.2 wt% Cu/*m*-ZrO_2 and 1.2 wt% Cu/*t*″-$Ce_{0.3}Zr_{0.7}O_2$ during the CO hydrogenation experiments presented in Figs. 8 and 9. The $\nu(CH_3)$ and $\nu_{as}(OCO)$ bands were used to track the development of CH_3O–Zr and b-HCOO–Zr species, respectively. Peak areas for both b-HCOO–Zr and CH_3O–Zr were normalized to the observed values after approximately 12 h. The concentration of formate species on 1.2 wt% Cu/*m*-ZrO_2 decreased rapidly from the level observed in the absence of gas phase H_2 during the first 15 min, before declining more slowly over the remainder of the transient. In contrast, the concentration of formate species reached a maximum at ~3 min on 1.2 wt% Cu/*t*″-$Ce_{0.3}Zr_{0.7}O_2$ before decreasing more slowly over the course of the experiment. The maximum formate concentration is attributed to the rapid hydrogenation of surface carbonate and/or carboxylate species to produce new formate groups, as evidenced by the rapid decline in the broad bands at ~1550–1450 and 1350–1250 cm^{-1}. Hydrogenation of carbonate species to formate species was previously observed during studies of CO_2 hydrogenation on Cu/ZrO_2 [70]. On both catalysts, the concentration of methoxide species increased rapidly from the levels observed during CO adsorption, reaching values within 95% of the steady-state concentration in <1 h.

The relative rates of consumption of formate and methoxide species were examined by switching from a CO/H_2 mixture to only H_2. Fig. 11 compares the dynamics of consumption of b-HCOO–Zr and CH_3O–Zr species on 1.2 wt% Cu/*m*-ZrO_2 and 1.2 wt% Cu/*t*″-$Ce_{0.3}Zr_{0.7}O_2$. Transient response spectra were obtained by replacing the 15% CO/He in the 3/1 H_2/CO flow with He while maintaining the total pressure at 0.50 MPa. Peak areas for both b-HCOO–Zr and CH_3O–Zr were normalized to the value observed at the beginning of the transient. The b-HCOO species decreased more rapidly initially on 1.2 wt% Cu/*m*-ZrO_2, al though the overall decrease in intensity was similar for both materials at the end of the transient. The concentration of CH_3O species decreased more rapidly on 1.2 wt% Cu/*t*″-$Ce_{0.3}Zr_{0.7}O_2$ than on 1.2 wt% Cu/*m*-ZrO_2, and there was a significant disparity in the relative concentra-

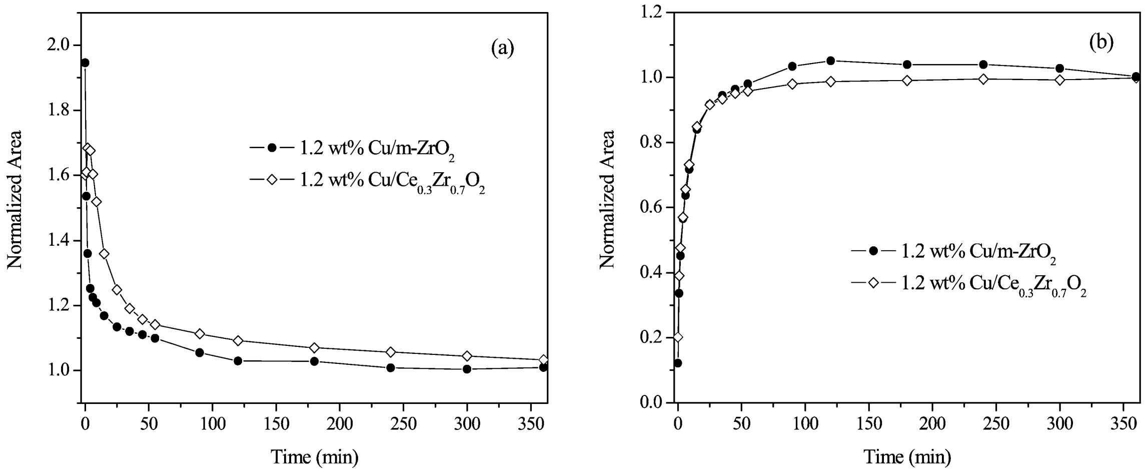

Fig. 10. Peak areas of (a) b-HCOO–Zr and (b) CH$_3$O–Zr features for 1.2 wt% Cu/*m*-ZrO$_2$ and 1.2 wt% Cu/Ce$_{0.3}$Zr$_{0.7}$O$_2$ during the experiments in Figs. 5.9 and 5.10. Areas normalized to the values observed at the end of the transient.

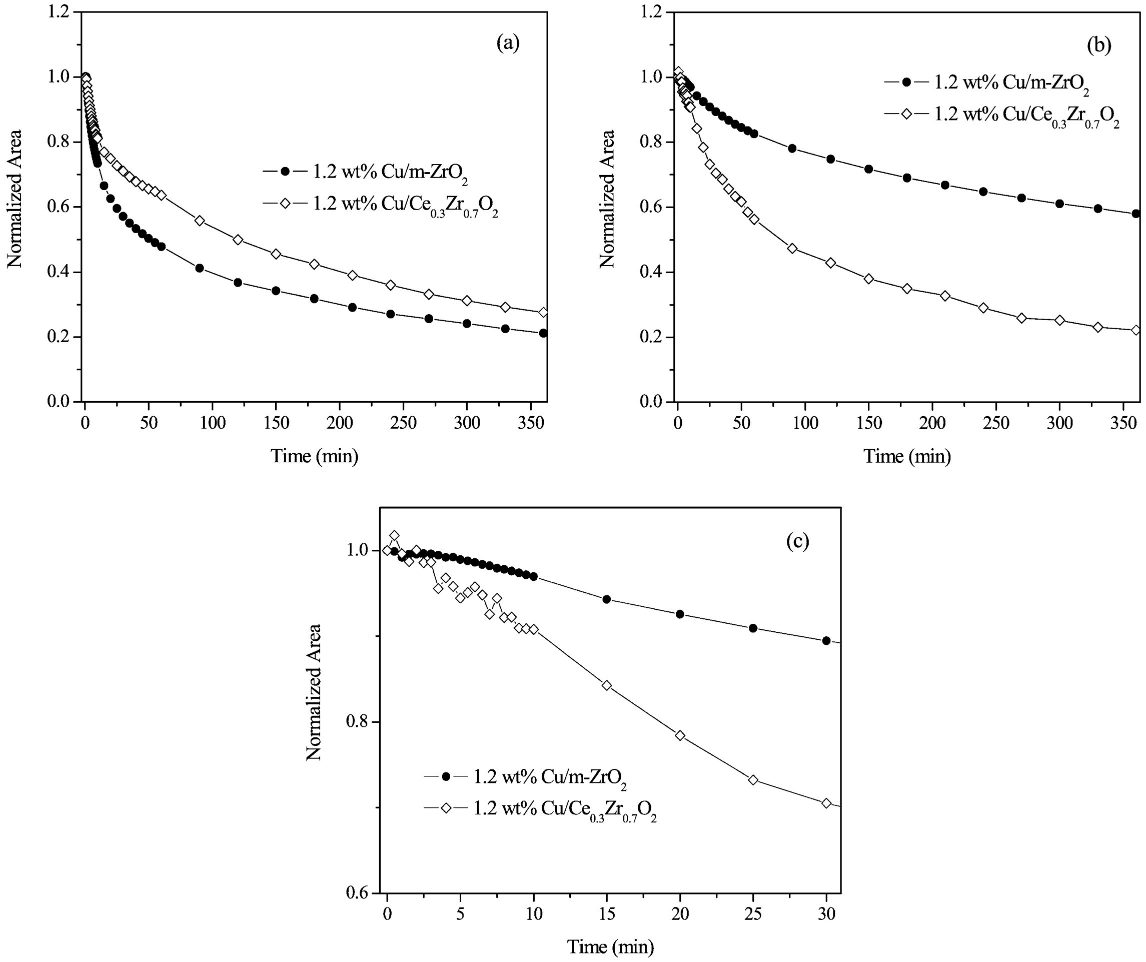

Fig. 11. Peak areas of (a) b-HCOO–Zr, (b) CH$_3$O–Zr, and (c) CH$_3$O–Zr features for 1.2 wt% Cu/*m*-ZrO$_2$ and 1.2 wt% Cu/Ce$_{0.3}$Zr$_{0.7}$O$_2$ at 523 K after switching feed from 0.05 MPa CO, 0.15 MPa H$_2$, and 0.30 MPa He to 0.15 MPa H$_2$ and 0.35 MPa He flowing at a total rate of 60 cm^3/min. Areas normalized to the values observed at the beginning of the transient.

tion of these species at the conclusion of the 6-h experiment. The initial decrease in methoxide species intensity also occurred more rapidly on 1.2 wt% Cu/t''-Ce$_{0.3}$Zr$_{0.7}$O$_2$ (∼2.5 min) than on 1.2 wt% Cu/*m*-ZrO$_2$ (∼4 min); see Fig. 11c. The apparent first-order rate constants for the removal of methoxide species, k_{app}, determined from the initial portion of the transient were 4.1×10^{-3} min^{-1} for 1.2 wt% Cu/*m*-ZrO$_2$ and 1.0×10^{-2} min^{-1} for 1.2 wt% Cu/t''-Ce$_{0.3}$Zr$_{0.7}$O$_2$.

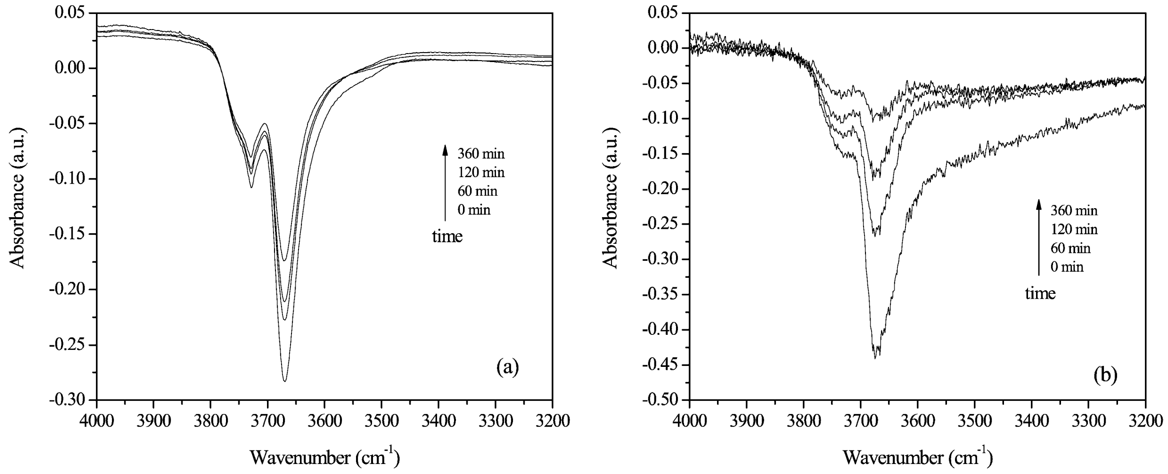

Fig. 12. Infrared spectra taken for (a) 1.2 wt% Cu/m-ZrO_2 and (b) 1.2 wt% Cu/$Ce_{0.3}Zr_{0.7}O_2$ at 523 K after switching feed from 0.05 MPa CO, 0.15 MPa H_2, and 0.45 MPa He to 0.15 MPa H_2 and 0.35 MPa He flowing at a total rate of 60 cm^3/min. Spectra referenced to 1.2 wt% Cu/m-ZrO_2 and 1.2 wt% Cu/$Ce_{0.3}Zr_{0.7}O_2$ under 0.50 MPa He flow at 523 K, respectively.

Fig. 12 shows the evolution of the O–H stretching region for both 1.2 wt% Cu/m-ZrO_2 and 1.2 wt% Cu/t''-$Ce_{0.3}Zr_{0.7}O_2$ during the H_2 reduction experiments presented in Fig. 10. Each material exhibited hydroxyl group consumption bands at ~3728 and ~3670 cm^{-1} at the conclusion of CO hydrogenation ($t = 0$ in Fig. 12). After the switch to an H_2-only feed, the bands decreased in negative absorbance over time, indicating a net recovery of hydroxyl groups over the course of the experiment. This is consistent with removal of formate and methoxide groups adsorbed at these sites during reaction through hydrogenation to methanol [5]. Notably, a greater portion of the hydroxyl groups on 1.2 wt% Cu/t''-$Ce_{0.3}Zr_{0.7}O_2$ was recovered during the course of the transient. Based on the changes in peak intensity, the recovery rates for hydroxyl groups after 6 h were ~35% on 1.2 wt% Cu/m-ZrO_2 and ~75% on 1.2 wt% Cu/t''-$Ce_{0.3}Zr_{0.7}O_2$. These values agree well with the fraction of methoxide species removed during the same experiment (see Fig. 12) (~42% on 1.2 wt% Cu/m-ZrO_2 and ~78% on 1.2 wt% Cu/t''-$Ce_{0.3}Zr_{0.7}O_2$), and suggest that most of the recovery in OH band intensity is associated with the removal of methoxide groups. Such a result would be expected from a consideration of the relative intensities of the band intensities for methoxide and formate species (see Figs. 8 and 9).

In their studies of methanol synthesis over Cu/t-ZrO_2 and Cu/m-ZrO_2, Bell et al. [13] established that the rate-limiting step is reductive elimination of Zr–OCH_3 species. As a result, the observed rate of methanol synthesis is proportional to the product of the apparent first-order rate coefficient for methoxide reductive elimination, k_{app}, and the surface concentration of methoxide groups, θ_{CH_3O}. The same reasoning can be used to interpret the higher rate of methanol synthesis on Cu/t''-$Ce_{0.3}Zr_{0.7}O_2$ relative to Cu/m-ZrO_2 observed in the present study. The values of k_{app} based on the initial data of the transient shown in Figs. 11b and c were 4.1×10^{-3} min^{-1} for 1.2 wt% Cu/m-ZrO_2 and 1.0×10^{-2} min^{-1} for 1.2 wt% Cu/t''-$Ce_{0.3}Zr_{0.7}O_2$. Hence the apparent rate coefficient was 2.4 higher for 1.2 wt% Cu/t''-$Ce_{0.3}Zr_{0.7}O_2$ than for 1.2 wt% Cu/m-ZrO_2. The higher value of k_{app} for the former catalyst is quite possibly due to the greater H_2 adsorption capacity of t''-$Ce_{0.3}Zr_{0.7}O_2$, because k_{app} is the product of the intrinsic rate coefficient for reductive elimination and the coverage of the oxide surface by H atoms. If the intrinsic rate coefficients on both catalysts were assumed to be the same, then the observed ratio of apparent coefficients would imply a 2.9 (corrected for the ratios of oxide surface areas) higher H-atom coverage on t''-$Ce_{0.3}Zr_{0.7}O_2$, which is consistent with the measured ratio in H_2 adsorption capacities (3.3). Based on the peak areas of the terminal and bridged methoxide C–O stretches, the ratio of methoxide species adsorbed on $Ce_{0.3}Zr_{0.7}O_2$ relative to ZrO_2 is 1.3 (corrected for the ratios of oxide surface areas) under steady-state reaction conditions. Hence, the ratio of the product $k_{app}\theta_{CH_3O}$ is ~3.8 in favor of 1.2 wt% Cu/t''-$Ce_{0.3}Zr_{0.7}O_2$. This figure is in reasonable agreement with the observed ratio of methanol synthesis activities (~2.7) once the measured rates are corrected for differences in the surface areas of the oxide and the dispersed Cu.

4. Conclusions

The activity for methanol synthesis from CO and H_2 of Cu/t''-$Ce_{0.3}Zr_{0.7}O_2$ is approximately two-fold higher than that for Cu/m-ZrO_2, assuming the same surface areas of the oxides and the dispersed Cu. Although Ce^{4+} cations replace Zr^{4+} cations isomorphously in the zirconia lattice during synthesis, the substituted cations are readily reducible to Ce^{3+}. The presence of Ce increases the adsorption capacity of the oxide for H atoms produced by dissociative adsorption of H_2 on the dispersed particles of Cu and spillover onto the oxide surface. The concentration of adsorbed methoxide species is also somewhat higher when Ce is substituted into the zirconium lattice. These two factors appear to account for the higher activity of Cu/t''-$Ce_{0.3}Zr_{0.7}O_2$.

Acknowledgments

This work was supported by the Director, Office of Basic Energy Sciences, Chemical Sciences Division, US Department of Energy under contract DE-AC03-76SF00098.

References

[1] J. Saussey, J.C. Lavalley, J. Mol. Catal. 50 (1989) 343.
[2] C. Schild, A. Wokaun, A. Baiker, J. Mol. Catal. 63 (1990) 243.
[3] S. Fujita, M. Usui, H. Ito, N. Takezawa, J. Catal. 157 (1995) 403.
[4] J. Weigel, R.A. Koeppel, A. Baiker, A. Wokaun, Langmuir 12 (1996) 5319.
[5] I.A. Fisher, A.T. Bell, J. Catal. 178 (1998) 153.
[6] G. Meitzner, E. Iglesia, Catal. Today 53 (1999) 433.
[7] B. Denise, R.P.A. Sneeden, Appl. Catal. 28 (1986) 235.
[8] Y. Sun, P.A. Sermon, J. Chem. Soc. Commun. (1993) 1242.
[9] Y. Sun, P.A. Sermon, Catal. Lett. 29 (1994) 361.
[10] I.A. Fisher, H.C. Woo, A.T. Bell, Catal. Lett. 44 (1997) 11.
[11] Y.W. Suh, S.H. Moon, H.K. Rhee, Catal. Today 63 (2000) 447.
[12] M.D. Rhodes, A.T. Bell, J. Catal. 233 (2005) 198.
[13] M.D. Rhodes, K.A. Pokrovski, A.T. Bell, J. Catal. 233 (2005) 210.
[14] M. Ozawa, J. Alloys Compd. 275–277 (1998) 886.
[15] J. Kašpar, P. Fornasiero, M. Graziani, Catal. Today 50 (1999) 285.
[16] T. Masui, T. Ozaki, K. Machida, G. Adachi, J. Alloys Compd. 303–304 (2000) 49.
[17] E. Mamontov, T. Egani, R. Brezny, M. Korrane, S. Tyagi, J. Phys. Chem. B 104 (2000) 11110.
[18] J. Kašpar, P. Fornasiero, J. Solid State Chem. 171 (2003) 19.
[19] M. Daturi, E. Finocchio, C. Binet, J.C. Lavalley, F. Fally, U. Perrichon, H. Vidal, N. Hickey, J. Kašpar, J. Phys. Chem. B 104 (2000) 9186.
[20] G. Vilac, R. Di Monte, P. Fornasiero, E. Fonda, J. Kašpar, M. Graziani, Catalysis and Automotive Pollution Control IV, Studies in Surface Science and Catalysis, vol. 116, Elsevier, Amsterdam, 1998.
[21] B.H. Toby, J. Appl. Crystallogr. 34 (2001) 210–213.
[22] S. Sato, R. Takahashi, T. Sodesawa, K. Yuma, Y. Obata, J. Catal. 196 (2000) 195.
[23] K.J. Sorenson, N.W. Cant, Catal. Lett. 33 (1995) 117.
[24] R.F. Hicks, C.S. Kellner, B.J. Savatsky, W.C. Hecker, A.T. Bell, J. Catal. 71 (1981) 216.
[25] C.E. Hori, H. Permana, K.Y. Simon Ng, A. Brenner, K. More, K.M. Rahmoeller, D.N. Belton, Appl. Catal. B 16 (1998) 105.
[26] C. Bozo, F. Gaillard, N. Guilhaume, Appl. Catal. A 220 (2001) 69.
[27] E. Tani, M. Yoshimura, S. Smiya, J. Am. Ceram. Soc. 66 (1983) 506.
[28] P. Duran, M. Gonzales, C. Moure, J.R. Jurdo, C. Pascal, J. Mater. Sci. 25 (1990) 5001.
[29] M. Yashima, H. Arashi, M. Kakihana, M. Yoshimura, J. Am. Ceram. Soc. 77 (1994) 1067.
[30] M. Yashima, K. Morimoto, N. Ishizawa, M. Yoshimura, J. Am. Ceram. Soc. 76 (1993) 1745.
[31] M. Yashima, K. Morimoto, N. Ishizawa, M. Yoshimura, J. Am. Ceram. Soc. 77 (1993) 2865.
[32] J.R. Ferraro, K. Nakamoto, Introductory Raman Spectroscopy, Academic Press, New York, 1994.
[33] C. Schild, A. Wokaun, R.A. Koeppel, A. Baiker, J. Catal. 130 (1991) 657.
[34] M. Li, Z. Feng, G. Xiong, P. Ying, Q. Xin, C. Li, J. Phys. Chem. B 105 (2001) 8107.
[35] C. Li, M. Li, J. Raman Spectrosc. 33 (2002) 301.
[36] A. Trovarelli, F. Zamar, J. Lorca, C. Leitenburg, G. Dolcetti, J.T. Kiss, J. Catal. 169 (1997) 490.
[37] V.S. Escribano, E.F. López, M. Panizza, C. Resini, J.M.G. Amores, G. Busca, Solid State Sci. 5 (2003) 1369.
[38] P. Fornasiero, G. Balducci, R. Di Monte, J. Kašpar, V. Sergo, G. Gubitosa, A. Ferrero, M. Graziani, J. Catal. 164 (1996) 173.
[39] S. Enzo, F. Delogu, R. Frattini, A. Primavera, A. Trovarelli, J. Mater. Res. 15 (2000) 1538.
[40] D. Martin, D. Duprez, J. Phys. Chem. B 101 (1997) 4428.
[41] K.D. Jung, A.T. Bell, J. Catal. 193 (2000) 207.
[42] M. Shimokawabe, H. Asakawa, N. Takezawa, Appl. Catal. 59 (1990) 45.
[43] R. Zhou, T. Yu, X. Jiang, F. Chen, X. Zheng, Appl. Surf. Sci. 148 (1999) 263.
[44] A. Trovarelli, G. Dolcetti, C. de Leitenburg, J. Kašpar, P. Finetti, A. Santoni, J. Chem. Soc., Faraday Trans. 88 (1992) 1311.
[45] S. Bernal, J.J. Calvino, G.A. Cifredo, A. Laachir, V. Perrichon, J.M. Herrmann, Langmuir 10 (1994) 717.
[46] C. de Leitenburg, A. Trovarelli, J. Kašpar, J. Catal. 166 (1997) 98.
[47] M. Boaro, M. Vicaro, C. de Leitenburg, G. Dolcetti, A. Trovarelli, Catal. Today 77 (2003) 407.
[48] C. Lamonier, A. Ponchel, A. D'Huysser, L. Jalowiecki-Duhamel, Catal. Today 50 (1999) 247.
[49] J.L.G. Fierro, J. Soria, J. Sanz, J.M. Rojo, J. Solid State Chem. 66 (1987) 154.
[50] M.Y. He, J.G. Ekerdt, J. Catal. 87 (1984) 381.
[51] J. Kondo, H. Abe, Y. Sakata, K. Maruya, K. Domen, T. Onishi, J. Chem. Soc., Faraday Trans. I 84 (1988) 511.
[52] W. Hertl, Langmuir 5 (1989) 96.
[53] E. Guglielminotti, Langmuir 6 (1990) 1455.
[54] D. Bianchi, T. Chafik, M. Khalfallah, S.J. Teichner, Appl. Catal. A 105 (1993) 223.
[55] H. Kalies, N. Pinto, G.M. Pajonk, D. Bianchi, Appl. Catal. A 202 (2000) 197.
[56] K. Pokrovski, K.T. Jung, A.T. Bell, Langmuir 17 (2001) 4297.
[57] J. Edwards, G. Schrader, J. Phys. Chem. 89 (1985) 782.
[58] M. Bensitel, V. Moravek, J. Lamonte, O. Saur, J.C. Lavalley, Spectrochim. Acta 43a (1987) 1487.
[59] D. Bianchi, T. Chafik, M. Khalfallah, S.J. Teichner, Appl. Catal. A 123 (1995) 89.
[60] F. Ouyang, J.N. Kondo, K. Maruya, K. Domen, J. Phys. Chem. B 101 (1997) 4867.
[61] F. Ouyang, J.N. Kondo, K. Maruya, K. Domen, Catal. Lett. 50 (1998) 179.
[62] C. Li, Y. Sakata, T. Arai, K. Domen, K. Maruya, T. Onishi, J. Chem. Soc., Faraday Trans. I 85 (1989) 929.
[63] T. Shido, Y. Iwasawa, J. Catal. 141 (1993) 71.
[64] E. Finocchio, M. Daturi, C. Binet, J.C. Lavalley, G. Blanchard, Catal. Today 52 (1999) 53.
[65] G. Jacobs, L. Williams, U. Graham, G.A. Thomas, D.E. Sparks, B.H. Davis, Appl. Catal. A 252 (2003) 107.
[66] G. Jacobs, P.M. Patterson, L. Williams, E. Chenu, D. Sparks, G. Thomas, B.H. Davis, Appl. Catal. A 262 (2004) 177.
[67] C. Li, Y. Sakata, T. Arai, K. Domen, K. Maruya, T. Onishi, J. Chem. Soc., Faraday Trans. I 85 (1989) 1451.
[68] A. Badri, C. Binet, J.C. Lavalley, J. Chem. Soc., Faraday Trans. 93 (1997) 1159.
[69] C. Binet, M. Daturi, Catal. Today 70 (2001) 155.
[70] I.A. Fisher, A.T. Bell, J. Catal. 172 (1997) 222.